Biogeosciences

Interannual sea–air CO$_2$ flux variability from an observation-driven ocean mixed-layer scheme

C. Rödenbeck[1], D. C. E. Bakker[2], N. Metzl[3], A. Olsen[4,5], C. Sabine[6], N. Cassar[7], F. Reum[1], R. F. Keeling[8], and M. Heimann[1]

[1]Max Planck Institute for Biogeochemistry, Jena, Germany
[2]School of Environmental Sciences, University of East Anglia, Norwich Research Park, Norwich, UK
[3]LOCEAN-IPSL, CNRS, Paris, France
[4]Geophysical Institute, University of Bergen and Bjerknes Centre for Climate Research, Bergen, Norway
[5]Uni Climate, Uni Research AS and Bjerknes Centre for Climate Research, Bergen, Norway
[6]NOAA Pacific Marine Environmental Laboratory, Seattle, USA
[7]Division of Earth and Ocean Sciences, Duke University, Durham, USA
[8]Scripps Institution of Oceanography, University of California, San Diego, USA

Correspondence to: C. Rödenbeck (christian.roedenbeck@bgc-jena.mpg.de)

Abstract. Interannual anomalies in the sea–air carbon dioxide (CO$_2$) exchange have been estimated from surface-ocean CO$_2$ partial pressure measurements. Available data are sufficient to constrain these anomalies in large parts of the tropical and North Pacific and in the North Atlantic, in some areas covering the period from the mid 1980s to 2011. Global interannual variability is estimated as about 0.31 Pg C yr^{-1} (temporal standard deviation 1993–2008). The tropical Pacific accounts for a large fraction of this global variability, closely tied to El Niño–Southern Oscillation (ENSO). Anomalies occur more than 6 months later in the east than in the west. The estimated amplitude and ENSO response are roughly consistent with independent information from atmospheric oxygen data. This both supports the variability estimated from surface-ocean carbon data and demonstrates the potential of the atmospheric oxygen signal to constrain ocean biogeochemical processes. The ocean variability estimated from surface-ocean carbon data can be used to improve land CO$_2$ flux estimates from atmospheric inversions.

1 Introduction

The ocean currently accounts for about half the sink of excess atmospheric CO$_2$ (Sarmiento et al., 2010). Long-term changes in this sink capacity, therefore, affect the climate change trajectory. While it is at present still hard to directly detect such trends in the available observations (e.g. McKinley et al., 2011), an understanding of underlying mechanisms may be gained by quantifying contemporary variations in sea–air CO$_2$ exchanges from the data, and relating them to driving influences. However, current information on interannual sea–air CO$_2$ flux variation and trends largely comes from biogeochemical process models (Wanninkhof et al. (2013) and references therein) and carries large uncertainties. While sea–air CO$_2$ flux variation can be estimated from atmospheric CO$_2$ data, the dominance of signals from land CO$_2$ fluxes in the atmospheric CO$_2$ records causes large uncertainties of the oceanic estimates (Peylin et al. (2013) and references therein). Surface-ocean data (CO$_2$ partial pressure) have proved to provide a more direct constraint in various studies focusing on regions relatively well covered by observations such as the tropical Pacific (e.g. Feely et al., 1999, 2002; Inoue et al., 2001; Ishii et al., 2014) or the North Atlantic (e.g. Watson et al., 2009; Telszewski et al., 2009; Schuster et al., 2013; Landschützer et al., 2013). For the global scale, Park et al. (2010) provided a data-based estimate of sea–air CO$_2$ flux variations by regression to the more densely observed variations of sea surface temperature (SST). As a complement, here we consider

the information about sea–air CO$_2$ flux variations directly contained in surface-ocean carbon data.

In a previous study (Rödenbeck et al., 2013), the spatio-temporal variability of sea–air CO$_2$ fluxes has been estimated based on the SOCAT database (Surface Ocean CO$_2$ Atlas v1.5, Pfeil et al., 2013) of surface-ocean CO$_2$ partial pressure measurements, using a diagnostic data-driven scheme of mixed-layer biogeochemistry. That study focused on seasonal variations, which were found to be well constrained from the data in most parts of the ocean. Estimated mean seasonal cycles are similar to the seminal climatology by Takahashi et al. (2009). In addition, the scheme also partly reproduces day-to-day variations through parameterizations in terms of sea surface temperature and a few other variables. Using phosphate observations, the plausibility of the scheme was tentatively confirmed on the seasonal timescale.

As a next step, we now also consider interannual variability (IAV). In particular, we consider the following questions:

- What are the main modes of interannual variability contributing to the global sea–air CO$_2$ flux?

- Not all parts of the ocean have been sampled frequently enough to reliably estimate interannual flux variations from the SOCAT data. In which parts of the ocean, and to what extent, does the available data coverage suffice to estimate interannual variations of the sea–air CO$_2$ flux?

- The ocean-internal processes (biology, transport) that add/remove dissolved inorganic carbon to/from the mixed layer, and thus cause anomalies in sea–air CO$_2$ fluxes, simultaneously also remove/add dissolved oxygen, leading to anomalies in the sea–air oxygen exchange and finally to tiny but detectable variations in the atmospheric oxygen abundance. Thus, regular atmospheric oxygen measurements contain information on ocean-internal biogeochemical processes (Keeling and Shertz, 1992). Using an atmospheric inversion technique, the atmospheric oxygen (and CO$_2$) observations at five sites operated since at least 1993 have been shown to be more or less sufficient to estimate interannual variations in the oceanic oxygen flux independently for at least three latitudinal bands (Rödenbeck et al., 2008). As the data-driven diagnostic mixed-layer scheme used here can be extended to calculate sea–air oxygen fluxes as well (by exploiting the above-mentioned link between the ocean-internal sources and sinks of carbon and oxygen), we can compare the SOCAT-based variations to those based on atmospheric oxygen. How consistent are these independent information sources?

We further compare the SOCAT-based estimates to an ocean process model simulation, and discuss the estimates in the context of an atmospheric CO$_2$ inversion.

2 Method

2.1 The data-driven mixed-layer scheme

This paper further analyses the spatio-temporal fields of surface-ocean CO$_2$ partial pressure (p^{CO_2}) and sea–air CO$_2$ flux presented in the companion paper Rödenbeck et al. (2013). As documented in detail there, these fields were estimated by fitting a simple diagnostic model of mixed-layer biogeochemistry to SOCAT p^{CO_2} data in the following way:

(1) A mixed-layer carbon budget equation (including simple parameterizations of sea–air CO$_2$ exchange (Wanninkhof, 1992; Naegler, 2009), solubility (Weiss, 1974), and carbonate chemistry (Sarmiento and Gruber, 2006), driven by observation-based environmental fields listed in Table 1) was used to express surface-ocean p^{CO_2} and sea–air CO$_2$ flux as a function of ocean-internal carbon sources and sinks (Fig. 1) for each pixel.

(2) A cost function was formed to measure the mismatch between the individual p^{CO_2} data points in SOCAT (binned into the scheme's pixels and time steps, see below) and the calculated p^{CO_2} field at the corresponding location and time.

(3) The ocean-internal carbon sources and sinks were adjusted so as to minimize this model–data mismatch. In order to interpolate areas/periods without data, additional smoothness constraints were applied (similar to those in the atmospheric inversion of Rödenbeck, 2005). The only difference of the present estimates with respect to Rödenbeck et al., 2013 is that we updated the data source to the shipboard observations[1] of SOCAT v2 (Pfeil et al., 2013; Bakker et al., 2014), offering data coverage until the end of 2011.

The calculation has been done on a global grid of $\approx 4° \times 5°$ pixels and daily time steps over 1985–2012 (inclusive). The first and last year will be discarded from any plots to avoid edge effects. Statistical analysis is done over 1993–2008 (inclusive) only, as this is a period with largest data coverage both in SOCAT v2 and in atmospheric oxygen records. To obtain interannual variations, we deseasonalize the time series by subtracting the mean seasonal cycle (1993–2008) and remove variations faster than about 1 year by a spectral filter corresponding to a Gaussian smoothing kernel (filter "Filt0.5gdas" of Rödenbeck, 2005).

2.2 Process contributions to variability

For any given location, the (interannual) variability of the sea–air CO$_2$ flux is the sum of two contributions:

---

[1]The high-frequency mooring and drifter observations available in recent years have been retained for independent validation (Supplement, Sect. S.4.2). This also provides a more uniform data density over time.

Table 1. Data sets used as driver fields in the parameterizations of sea–air gas exchange, solubility, and carbonate chemistry (see Rödenbeck et al., 2013).

Quantity	Data set	Reference
Wind speed	NCEP reanalysis	Kalnay et al. (1996)
Sea surface temperature	OAFlux	Yu and Weller (2007)
Ice-free fraction	OAFlux	Yu and Weller (2007)
Mixed-layer depth (climatology)	LOCEAN	de Boyer Montégut et al. (2004)
Salinity (climatology)	WOA 2001	Conkright et al. (2002)
Alkalinity (climatology)		Lee et al. (2006)
Buffer factor		Egleston et al. (2010)
Reference DIC concentration	GLODAP	Key et al. (2004)

Glossary: GLODAP = Global Ocean Data Analysis Project; LOCEAN = Laboratoire d'océanographie et du climat: expérimentations et approches numériques; NCEP = National Centers for Environmental Prediction; OAFlux = Objectively Analysed air–sea Fluxes; WOA = World Ocean Atlas.

Contribution OIS (ocean-interior sources/sinks)

Variations in biological conversion and/or ocean transport into the mixed layer lead to anomalous ocean-internal sources/sinks f_{int}^{DIC} of dissolved inorganic carbon (DIC) (Fig. 1, bottom), which then lead to enhanced/reduced sea–air CO_2 fluxes $f_{ma}^{CO_2}$ (Fig. 1, top). The responses in $f_{ma}^{CO_2}$ are, however, of smaller magnitude than and delayed with respect to the causes in f_{int}^{DIC} because the buffering capacity of carbonate chemistry (Revelle factor) strongly enhances the limiting effect of the finite gas exchange velocity.

Contribution TE (thermally induced exchange)

Even in the absence of ocean-internal sources or sinks, the sea–air flux varies in response to temperature-induced changes in solubility and chemical equilibrium[2] (plus minor contributions from changes in atmospheric pressure, freshwater effects, and alkalinity). Contribution TE also comprises a secular CO_2 uptake (and consequent rise of p^{CO_2}) induced by the prescribed rising atmospheric CO_2 content.

Both contributions are somewhat modulated by variations in gas exchange (Supplement, Sect. S6) and mixed-layer depth.

In the diagnostic scheme, contribution TE is considered known from the employed process parameterizations driven by observed variables (predominantly SST). In contrast, the ocean-internal DIC sources/sinks f_{int}^{DIC} causing contribution OIS are taken as unknowns, to be adjusted in such a way that the total variations in the CO_2 partial pressure (sum of

Sea–air CO_2 flux:

Surface-ocean CO_2 partial pressure:

Mixed-layer DIC concentration:
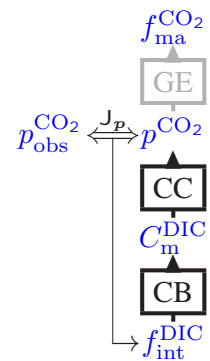
Ocean-internal DIC sources/sinks:

Figure 1. Illustration of the inverse procedure in our main case (run **SFC**); boxes denote the process representations causally linking quantities from bottom to top: mixed-layer carbon budget (CB), carbonate chemistry (CC), solubility and sea–air gas exchange (GE). The double arrow symbolizes the matching between observed and modelled CO_2 partial pressure, as gauged by the cost function J_p. The thin arrow indicates the adjustments of the unknown ocean-internal carbon sources/sinks, undertaken to minimize the model–data mismatch (see Rödenbeck et al. (2013) for full details).

contributions OIS and TE) are compatible with the SOCAT data (for illustration see also Fig. 3 of Rödenbeck et al., 2013). The Bayesian prior is chosen to be $f_{int}^{DIC} = 0$, such that any positive or negative anomalies in the ocean-internal sources/sinks are a priori equally likely, i.e. we do not assume any prior knowledge on the ocean-internal processes. Consequently, the prior of the sea–air flux coincides with contribution TE.

2.3 Performance diagnostics

2.3.1 Reduction of uncertainty (RoU)

As the main diagnostic to identify which regions are well constrained by the data, we use the "reduction of uncertainty" (RoU), a standard diagnostic of Bayesian estimation defined

---

[2] Though contribution TE is mainly driven by the "thermal component of p^{CO_2}" considered in the literature (Takahashi et al., 2009), its temporal course differs from that of SST because, besides the static dependence of p^{CO_2} on temperature, it also takes into account the dynamic response of the mixed-layer DIC content: temperature rise(decline) induces out(in)gassing fluxes which counteract the direct temperature effect. As a consequence of this balance, peaks in the TE contribution tend to be related to temperature changes and thus occur earlier than the actual temperature peaks.

as

$$\text{RoU} = 1 - \frac{\sigma_{\text{post}}}{\sigma_{\text{pri}}} \qquad (1)$$

with σ_{pri} and σ_{post} denoting the formal a priori and a posteriori uncertainties of the flux. High values (RoU towards 1) indicate strong data constraints, while low values (close to 0) indicate that the data are not able to move the estimates away from the prior.

The uncertainty intervals σ_{pri} and σ_{post} have been calculated statistically from an ensemble of $n = 50$ inversion runs with pseudorandom realizations of a priori errors and model–data mismatch errors: in each inversion run, prior and data have been replaced by values drawn according to their specified (co)variances using a Gaussian pseudorandom number generator (in the case of the prior, pseudorandom numbers with the full a priori covariance structure are obtained from independent Gaussian pseudorandom numbers using the "flux model formulation" Eq. (3) of Rödenbeck, 2005). Exploiting the linearity of the inversion problem, each member i of the pseudorandom ensemble then gives a realization $\Delta_i f_{\text{post}}$ of the a posteriori error of the flux field. The uncertainties σ_{pri} and σ_{post} are thus given by the root mean square of the error fields across the ensemble, $\sigma = \sqrt{\sum_i (\Delta_i f)^2 / n}$ (as the expectation value of the error is 0 by construction). As we want to obtain RoU specifically for interannual variations (and possibly for regional averages), the a priori and a posteriori error fields of each ensemble member are interannually filtered (and regionally averaged) in the same way as the actual flux estimates, before the root mean square is calculated. That way, any covariances between the a posteriori errors at different locations/times are automatically taken into account.

Of course, the root mean square across the finite ensemble only gives an approximation to the uncertainty intervals. For our sample size of 50, standard deviations could be a factor of 0.79 smaller or a factor of 1.34 larger (confidence interval for a confidence level of 99 %). Calculated RoU values can, therefore, only give the 1st-order pattern of the strength of the data constraint. When calculating the overall performance over a given time period, however, we increased the sample size (and thus improved the statistics) by calculating the root mean square error not only across the ensemble but also across all monthly values of the flux error realizations within that period (method proposed by Chevallier et al., 2007).

2.3.2 Test of independence from IAV in the drivers

Most driving variables of the mixed-layer scheme (in particular SST) also contain interannual variations. If a region is well constrained with respect to IAV, however, then the IAV of the estimated p^{CO_2} field should only depend on the signals in the p^{CO_2} data, "overwriting" any influence of IAV in the drivers of the parameterizations (remember that the scheme does not involve any regression to these drivers). We thus performed a test run in which any IAV has been removed from the driver variables (except for a linear rising trend in atmospheric CO$_2$). In well-constrained regions the result will be similar to the standard result. We use this as a qualitative confirmation to the RoU diagnostic.

It should be noted that, for quantities other than the p^{CO_2} field, IAV in the drivers can of course be important also in well-constrained regions, for example IAV in wind speed that influences sea–air CO$_2$ fluxes.

2.3.3 Synthetic data test

Another traditional method to assess the strength of the data constraint (also used in Rödenbeck et al. (2013) for seasonality) is "synthetic data tests", where (1) a modelled p^{CO_2} field is sampled at the locations/times of the SOCAT data to create a synthetic data set, and (2) a p^{CO_2} field is retrieved by the diagnostic mixed-layer scheme from the synthetic data and compared to the original modelled field as the known "true" answer. However, this method is dependent on the particular time course of the chosen synthetic "truth", confounding any information about the temporal changes in the strength of the constraint. Despite its higher computational demand, we therefore prefer the RoU diagnostic (Sect. 2.3.1) here. Nevertheless, synthetic data tests have been performed to check consistency with the RoU diagnostic (not shown).

2.3.4 Sensitivity tests

In addition to gaps in data coverage, results may be affected by uncertainties in parameters or input data sets used in the calculation. To assess these errors, we performed a series of sensitivity runs varying those parameters that are considered most uncertain: (i) increase and decrease of the a priori uncertainty by a factor of 2, leaving more/less freedom to inverse adjustments, (ii) decrease of the a priori uncertainty of nonseasonal variations in $f_{\text{int}}^{\text{DIC}}$ by a factor of 2, (iii) decrease in the spatial correlation lengths in latitude direction by a factor of 2, (iv) increase and decrease of the global mean piston velocity by 3.2 cm h^{-1} (range given by Naegler, 2009) or using a cubic dependence of piston velocity on wind speed (still keeping the global mean piston velocity at the value from Naegler, 2009), and (v) increase and decrease of the mixed-layer depth h by a factor of 2. As all these changes are still considered reasonable values, the envelope of these sensitivity results (the range between the smallest and largest value at each time) gives a lower bound for the error (to be plotted as grey bands in the figures in this paper).

2.3.5 Residuals and comparison to independent time series

As a consistency check of the fit, residuals between the estimated p^{CO_2} field and the SOCAT data are assessed. According to the Supplement (Sect. S4.1), the data are fitted within

10 to 15 µatm (root-mean-squared residuals), consistent with the assumed mismatch uncertainty. Any remaining interannual signals in the residuals are negligible, confirming that the data information is used in its entirety.

Short-term variations are further validated against high-frequency time series from various moorings not used in the fit (Supplement, Sect. S4.2). For testing interannual variations, independent continuous long-term surface-ocean carbon time series are used (Supplement, Sect. S4.3).

2.4 Lagged correlation analysis

To assess the relation of estimated interannual flux anomalies to El Niño–Southern Oscillation (ENSO), we correlate them to the Multivariate El Niño Index (MEI) by Wolter and Timlin (1993). The MEI has been interannually filtered in the same way as the flux (Sect. 2.1). The correlation is calculated for different time lags between flux and the MEI; we always report the maximum correlation coefficient. Where local maxima exist for several lags, we choose the smallest absolute lag.

Correlations have been calculated over the 1993–2008 analysis period. Assuming each of these 16 years to be statistically independent (because the interannual filter is roughly equivalent to yearly averages), correlations are moderately significant (at the 90 % level) if their correlation coefficient exceeds 0.50.

2.5 Calculating sea–air oxygen fluxes

In order to relate the SOCAT-based variability estimates to inverse estimates by Rödenbeck et al. (2008) based on atmospheric oxygen data, we extend the diagnostic mixed-layer scheme in three steps.

2.5.1 Ocean-internal oxygen sources/sinks

The ocean-internal processes (biology, transport) that add or remove dissolved inorganic carbon to/from the mixed layer also add or remove dissolved oxygen (symbolized as box "TT" in Fig. 2). Biological respiration and photosynthesis lead to opposite, mutually proportional changes in carbon and oxygen that we assume to follow a fixed Redfield stoichiometry. Mixing of water from the ocean interior into the mixed layer can change its carbon and oxygen concentrations as well. These transport-induced changes do not follow a simple stoichiometry, but analysis of vertical tracer gradients suggests that their mutual relation is also roughly in Redfield proportions. We therefore assume

$$f_{int}^{O_2} = r_{O_2:C} \cdot f_{int}^{DIC} \tag{2}$$

with the Redfield ratio $r_{O_2:C} = -150/106 \approx -1.4$ (Anderson, 1995) as an approximation.
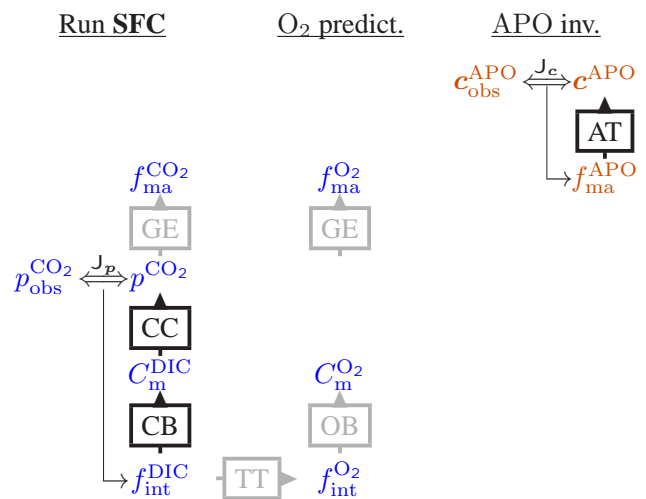

Figure 2. Information flow between carbon and oxygen variables. Left: inverse procedure of run **SFC** as in Fig. 1, estimating ocean-internal DIC sources/sinks from $p_m^{CO_2}$ data. Middle: prediction of the oxygen sea–air flux; ocean-internal oxygen sources/sinks are calculated from DIC sources/sinks via tracer–tracer coupling (TT) assumed to follow Redfield stoichiometries; dissolved oxygen concentration ($C_m^{O_2}$) and sea–air oxygen flux ($f_{ma}^{O_2}$) are then obtained from parameterizations of a mixed-layer oxygen budget (OB), as well as oxygen solubility and sea–air gas exchange (GE), analogous to those for carbon. Right: APO inversion of Rödenbeck et al. (2008); sea–air APO fluxes are estimated from APO observations (combined atmospheric oxygen and CO_2 data) by inversion of atmospheric transport (AT).

2.5.2 Sea–air oxygen fluxes

Sea–air oxygen fluxes $f_{ma}^{O_2}$ are calculated from $f_{int}^{O_2}$ (Eq. 2) using parameterizations of the mixed-layer oxygen budget and sea–air oxygen exchange (Fig. 2, middle column). These oxygen parameterizations are analogous to those of carbon (left column) detailed in Rödenbeck et al. (2013), except that (i) different coefficients are used in the calculation of solubility and Schmidt number (see Supplement of Rödenbeck et al., 2013), (ii) there is no equivalent to carbonate chemistry involved, and (iii) sea–air oxygen exchange contains an additional contribution from air injection through bubbles[3].

---

[3]Gas injection by bubbles is parameterized by

$$f_{bubb}^{O_2} = X^{O_2} \cdot f_{bubb}^{Air} \tag{3}$$

with the oxygen mixing ratio $X^{O_2} = 209392$ ppm. This assumes complete dissolution of bubbles (shown to be the dominating process; Stanley et al., 2009). The air injection flux (positive for injection into the ocean) is taken to depend on wind speed u according to Monahan and Torgersen (1990):

$$f_{bubb}^{Air} = \begin{cases} B(u - u_0)^3 \dfrac{p_{baro}}{R_{gas}(T + T_0)}, & u > u_0 \\ 0, & \text{else} \end{cases} \tag{4}$$

2.5.3 Atmospheric Potential Oxygen (APO) fluxes

The use of atmospheric oxygen data involves the complication that the atmospheric oxygen abundance is also influenced by oxygen exchanges from the land biosphere. To account for that, the inversion (Rödenbeck et al., 2008) has not been applied to oxygen itself but to the conceptual tracer "atmospheric potential oxygen" (APO) introduced by Stephens et al. (1998). APO is defined as a combination of O$_2$ and CO$_2$ abundances in such a way that its surface-to-atmosphere fluxes are

$$f^{APO} = f^{O_2} + 1.1 \cdot f^{CO_2}. \tag{5}$$

As O$_2$ exchanges from the land biosphere are, to good approximation, -1.1 times the CO$_2$ exchanges, they cancel each other in the APO flux. There is a remaining contribution from fossil fuel burning as it has a slightly different stoichiometry (about -1.4, Keeling, 1988), but this contribution has been accounted for in the APO inversion based on fuel-use statistics (see Rödenbeck et al., 2008). Thus, the APO inversion yields an estimate of the oceanic APO flux f_{ma}^{APO}.

The comparison is therefore done in terms of f_{ma}^{APO}. The SOCAT-based APO flux has been calculated according to Eq. (5) from the (dominant) oxygen contribution $f_{ma}^{O_2}$ obtained as described above and the (small) carbon contribution $f_{ma}^{CO_2}$ directly available from the **SFC** calculation. The atmospheric inversion of Rödenbeck et al. (2008) has been updated by adding more recent observations to extend the time period to the end of 2011.

3 Results and discussion

3.1 Overview

While the sea–air CO$_2$ flux varies on interannual, seasonal, and day-to-day timescales (Fig. 3, top), this paper focuses on interannual anomalies of the sea–air CO$_2$ flux around its mean (filtered flux, bottom). The largest contributions to the global interannual variability (IAV) are estimated to come from the subpolar North Pacific and Atlantic, the tropical Pacific, and parts of the Southern Ocean (Fig. 4, top). Due to

---

with the threshold wind speed $u_0 = 2.27\,\mathrm{m\,s^{-1}}$, barometric pressure p_{baro}, gas constant $R_{gas} = 8.3144\,\mathrm{J\,mol^{-1}\,K^{-1}}$, and absolute temperature $T + T_0$. The global constant B has been calculated such that the global diffusive gas exchange $f_{ge}^{O_2}$ calculated from the World Ocean Atlas (WOA) climatology of surface-ocean dissolved oxygen (Garcia et al., 2006) equals the global bubble injection flux, such that the long-term global sea–air oxygen flux is 0.

It should be noted that the bubble flux has only very little influence on the sea–air oxygen fluxes calculated here from internal O$_2$ sources and sinks: due to the fast equilibration of dissolved oxygen with the atmosphere (within less than a month), the oxygen input by bubbles is essentially compensated for (on interannual timescales) by a corresponding enhancement in the diffusive sea–air oxygen exchange.
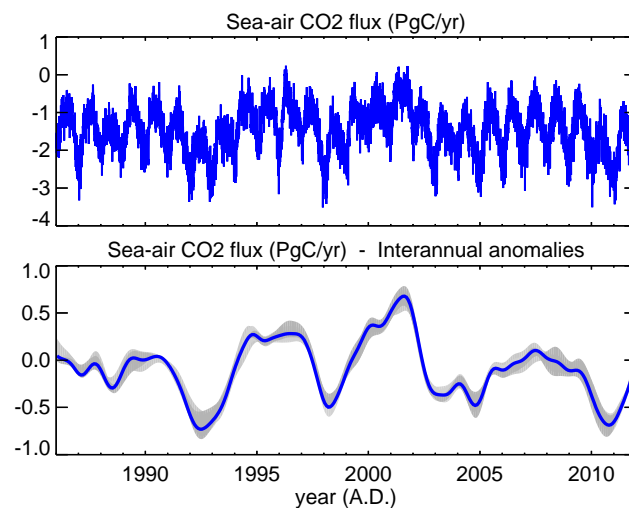

Figure 3. Top: globally integrated sea–air CO$_2$ exchange estimated from SOCAT data (run **SFC**, blue). Negative values indicate an ocean CO$_2$ sink. Bottom: interannual anomalies of the globally integrated sea–air CO$_2$ exchange. The time series have been deseasonalized and filtered for interannual variations, and the 1993–2008 mean flux has been subtracted (positive values indicate an increased ocean CO$_2$ source or a decreased sink). The light grey band around the standard case comprises a set of sensitivity cases (Sect. 2.3.4). The time period shown excludes the first year for spin-up and the years after the end of SOCAT v2 (end of 2011).

its large size and its spatially coherent variations, the tropical Pacific (15° S–15° N) provides the largest contribution (Fig. 5, top), with a temporal standard deviation of about 40 % of that of the global ocean[4]. Consistent with the literature (e.g. Feely et al., 1999; Inoue et al., 2001; Feely et al., 2002), the sea–air CO$_2$ flux anomalies are strongly tied to El Niño–Southern Oscillation (ENSO), with a reduced CO$_2$ source during El Niño phases (see Sect. 3.4 below).

3.2 Strength of the data constraint on IAV

To identify which parts of the ocean have been sampled frequently enough to reliably estimate interannual flux variations from the SOCAT data, Fig. 4 (bottom) shows the "reduction of uncertainty" (RoU) defined in Sect. 2.3.1. It indicates the strength of the data to detect deviations of the flux from its climatological mean. Good constraints (larger RoU) are found in the tropical and North Pacific and in the North Atlantic, highlighting the large long-running observational programs by US, Japanese, and European research groups. Specifically, the locations of the repeated cruises crossing the Equator are seen, as well as the ship routes traversing the North Atlantic. In contrast, poor constraints (low RoU, even below the arbitrary threshold of 0.2 left uncoloured in

---

[4]Over 1993–2008, the global standard deviation is about 0.31 Pg C yr^{-1} and that of the tropical Pacific is 0.13 Pg C yr^{-1}.
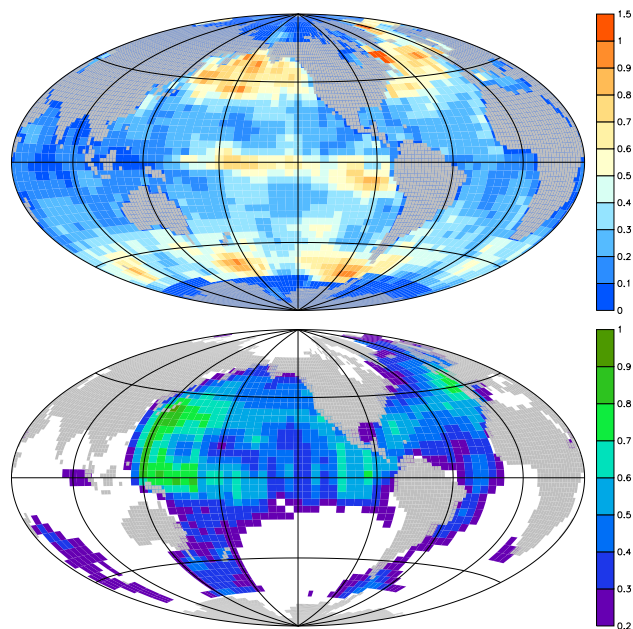
Figure 4. Top: amplitude of IAV of the sea–air CO_2 flux estimated from SOCAT data (run **SFC**), calculated as temporal standard deviation (1993–2008) of the interannually filtered flux (μmol m^{-2} yr^{-1}). Bottom: capacity of the diagnostic scheme to retrieve interannual variations in the sea–air CO_2 flux from SOCAT v2 data (reduction of uncertainty, average performance 1993–2008). Pixels with RoU < 0.2 have been left white.

the map) prevail in the Indian Ocean and most parts of the Southern Hemisphere extratropical ocean.

Figure 4 (bottom) gives the overall performance within 1993–2008. Depending on the region considered, this period may comprise both well constrained and badly constrained years (Supplement, Fig. S1). For example, the RoU in the extratropical North Atlantic clearly increased after the implementation of the p^{CO_2} observing network in the first half of the 2000s (Watson et al., 2009) and has remained steady at between approximately 0.6 and 0.8 since then.

In well-constrained regions/periods (high RoU), estimated interannual anomalies are essentially independent of the prior. For example, the data are able to almost reverse the a priori anomalies in the tropical Pacific (Fig. 5). Strong constraints in the tropical Pacific in many years are further confirmed by a test run without interannual variations in all driving variables (Sect. 2.3.2): even though the prior correspondingly loses almost all its interannual variability, the estimated p^{CO_2} anomalies hardly change (supplementary Sect. S2). In contrast, poorly constrained regions (low RoU) stay close to the prior (Supplement, Fig. S1). In areas where the temperature-related variability (contribution TE contained in the prior, Sect. 2.2) dominates IAV, the results of the diagnostic mixed-layer scheme may still capture part of the real IAV, otherwise the variability from the ocean-internal fluxes (contribution OIS) is missing there.
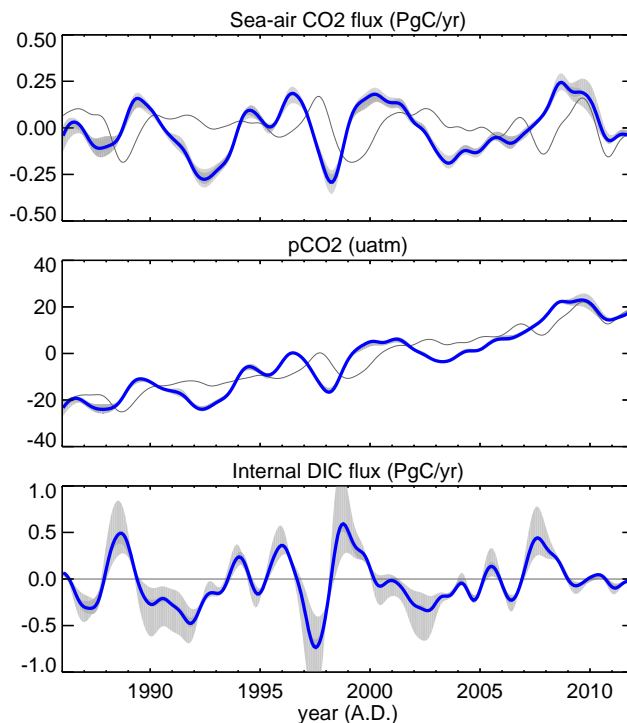

Figure 5. Interannual carbon anomalies in the tropical Pacific (15° S–15° N) from run **SFC** (blue; filter, grey uncertainty band, and sign convention as in Fig. 3). Top: sea–air CO_2 flux anomalies ($f_{ma}^{CO_2}$). Middle: surface CO_2 partial pressure anomalies (p^{CO_2}). Bottom: anomalies in the ocean-internal DIC sources and sinks (f_{int}^{DIC}, note that the vertical scale is different from $f_{ma}^{CO_2}$). The dark grey lines give the a priori state of the diagnostic scheme, which only responds to changes in the driving variables (predominantly temperature).

The pattern of RoU shown in Fig. 4 is similar to the map of the number of data points (Supplement, Fig. S7.4, of Rödenbeck et al., 2013), but additionally takes into account that any data point in an already well-covered area has less individual effect. Though RoU is to some extent also influenced by our a priori uncertainty settings (e.g. a smaller a priori uncertainty would lower the achievable RoU, and the applied smoothness constraints carry information into unconstrained areas close to constrained ones), the patterns of Fig. 4 (bottom) should be broadly representative for SOCAT's information content on interannual anomalies, largely independently of the method used here.

3.3 Robustness

To exclude that the results are dominated by uncertain parameters or input data sets used in the calculation, Fig. 5 shows the envelope of a set of sensitivity results (Sect. 2.3.4), using the tropical Pacific as example region. Reflecting the fact that p^{CO_2} (middle panel) is the quantity directly constrained by the data, alterations in parameters only have a very small

effect (the sensitivity band is much narrower than the interannual variations). There are short periods of enhanced sensitivity in 2009 and before about 1992, when the tropical Pacific is less well constrained by the SOCAT data, such that it stays closer to the prior, meaning that the effects of our sensitivity cases on the prior cannot be completely overwritten.

The sensitivity of the sea–air CO_2 fluxes (Fig. 5, top) is slightly enhanced compared to that of p^{CO_2}, due to the cases with altered gas exchange velocity directly affecting the flux. Still, despite some change in amplitude, the time course of the interannual flux variations is very robust.

Larger sensitivity is found in the ocean-internal DIC sources/sinks (Fig. 5, bottom). This is expected as any alteration in the parameterized relation between f_{int}^{DIC} and p^{CO_2} enforces compensating changes in f_{int}^{DIC}. The biggest effect on f_{int}^{DIC} comes from the alterations in mixed-layer depth (MLD). Note however that our alterations of MLD (as of Table 1) by constant factors 2 and 0.5 are ad hoc; this large range has been chosen to account for the missing interannual variations in MLD values used but may overestimate the actual MLD errors.

In regions less well constrained than the tropical Pacific, estimates are less robust. Besides the above-mentioned effect that the alterations of the prior have more impact on the result, estimates in unconstrained regions critically depend on the choice of spatial correlation length: the longer the correlations, the farther variability from data-constrained locations is spread into unconstrained locations (see Fig. 5 of Rödenbeck et al., 2013). In particular, longer correlations carry the strong variability of the tropical Pacific farther into the poorly constrained areas south of it (Fig. 4, bottom), thus increasing the areal extent of this variability and leading to higher global IAV[5]. This leads to a sensitivity band for the global sea–air CO_2 fluxes (Fig. 3, bottom) that is somewhat wider than in the tropical Pacific. As the band is asymmetric, it suggests a somewhat lower amplitude of global IAV than in the standard case.

3.4 Interannual variability in the tropical Pacific

As the presented material establishes that the tropical Pacific is both a well-constrained and a globally important contributor to interannual sea–air CO_2 flux variability[6], we consider the contributions to the variability at different longitudes along the Equator (Fig. 6). During the 1993–2008 analysis period, fluxes at most longitudes are continuously constrained (left panel); in the western part this is the case even in the earlier years. The reduction of the flux during El Niño phases (middle, red colours) extends throughout the considered part of the equatorial Pacific (200 to 85° W), but with the tendency to be of smaller amplitude and to occur several months later in the east than in the west. This striking "propagation" can be confirmed statistically: the flux is significantly anti-correlated (Sect. 2.4) to the MEI (Wolter and Timlin (1993); interannually filtered) at almost all longitudes (middle right panel, dark blue line), with a time lag increasing by more than half a year from west to east (top right panel; also see the example time series in the Supplement, Fig. S6, for illustration).

Such a slow west-to-east "propagation" of sea–air CO_2 flux anomalies as constrained by SOCAT is not present in physical surface-ocean variables: for example, SST is positively correlated to the MEI with almost no lag and propagating much faster (within about 1 month, consistent with an equatorial Kelvin wave; not shown).[7] No slow "propagation" is thus found in the SST-dominated TE contribution either: consistent with Footnote 2 on page 3, the TE contribution is positively correlated to the MEI as well (middle right panel, black line) and leads the MEI by about 4 months at most longitudes (top right panel). However, the OIS contribution (calculated by difference; light blue) also shows a west-to-east "propagation" of only 1–2 months. This suggests that the slow "propagation" of the total anomalies is only an apparent one and does not arise from any actual propagation mechanism. Rather, as the amplitudes of the opposite TE and OIS contributions are markedly changing from west to east (bottom right panel), the temporal phase of their superposition is shifting (in the same way as sine and cosine Fourier terms of different relative weights add up to modes with different phases).

---

[5]The chosen length scale reflects both the size of coherent El Niño-related variations and the available information: even in the well-constrained equatorial Pacific, sufficient data coverage only exists at every 15° longitude (see Fig. 4, bottom) – if a shorter correlation scale is used, areas in between nearly revert back to the prior, leading to much smaller variations in the regional flux. Bridging these gaps through the correlations is justified as we expect longitudinally coherent variations here. In latitude direction, shorter correlation lengths are chosen, reflecting the narrow size of El Niño-related features. Unfortunately, as the data coverage rapidly drops south of the equatorial region, both longer and shorter latitudinal correlation lengths lead to results equally compatible with the SOCAT data (they have similarly low residual bias; not shown), despite their differences in the IAV amplitude of the regional (or global) total.

---

[6]Ocean regions other than the tropical Pacific either have much less IAV or are not well constrained by the available p^{CO_2} observations (Supplement, Fig. S1). Comparison with independent data at station HOT in the North Pacific broadly confirms the SOCAT-based anomalies, including the low IAV there (Supplement, Sect. S4.3). Comparison at BATS is not successful in terms of interannual features but still confirms the low amplitude in the North Atlantic as well (Supplement, Sect. S4.3). Despite their lower IAV, various extratropical regions can be expected to play an important role in the long-term flux trend. A more detailed consideration warrants a separate study.

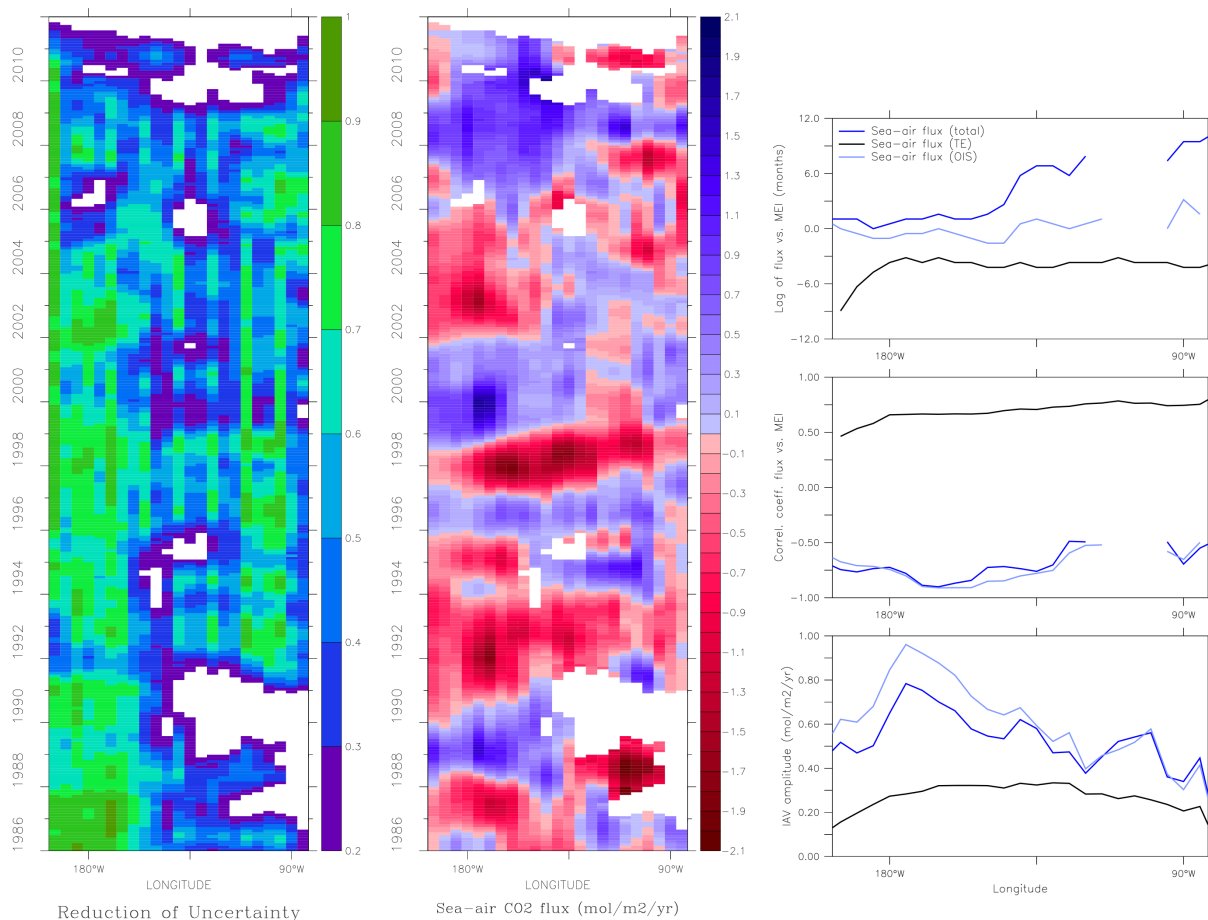[7]In weak ENSO events, SST anomalies can even propagate westward; see Santoso et al. (2013).

Figure 6. Sea–air CO$_2$ flux variability along the Equator in the Pacific (4° S–4° N average). Left: strength of the data constraint (RoU). Middle: interannual anomalies of sea–air CO$_2$ flux shown as Hovmöller plot (colour-coded over longitude (horizontal axis) and time (vertical axis); locations/periods with RoU < 0.2 left white). Right: statistical properties (calculated for 1993–2008): time lag at which the flux is most strongly correlated to El Niño (interannually filtered MEI; Wolter and Timlin, 1993) (upper panel, positive values mean that the flux trails the MEI); correlation coefficient at this time lag (middle panel); and temporal standard deviation of interannual flux anomalies (lower panel). In the correlation plots, insignificant correlations have been discarded. (The Supplement, Fig. S6 in Sect. S3, illustrates correlations and time lags again in a time series view.)

Can the remaining "propagation" in the OIS contribution arise from memory effects in the mixed-layer carbon budget? Anomalies in contribution OIS occur several months later than the anomalies in the ocean-interior DIC sources/sinks that cause them (not shown, but see the Supplement, Fig. S6), due to the finite sea–air exchange rate enhanced by the buffer effect of carbonate chemistry. Anomalies in f_{int}^{DIC} thus even lead the MEI by 5–6 months, ie. are associated with the build-up or decline of the ENSO states. However, this delay between f_{int}^{DIC} and $f_{ma}^{CO_2}$ is essentially the same throughout the equatorial Pacific, ie. it does not contribute to the propagation.

3.5   Consistency with atmospheric oxygen observations

In order to relate the SOCAT-based IAV estimates to the information from atmospheric oxygen, the oceanic APO

flux has been calculated from run **SFC** (Sect. 2.5). The information flow is illustrated in Fig. 7. Sea–air CO$_2$ flux ($f_{ma}^{CO_2}$, middle left) and ocean-interior carbon sources/sinks (f_{int}^{DIC}, bottom left) are the quantities constrained by SO-CAT. Ocean-interior sources/sinks of oxygen ($f_{int}^{O_2}$, bottom right) are implied by those of carbon in the assumed Redfield proportion. Due to the short equilibration time of oxygen, anomalies in sea–air O$_2$ exchanges ($f_{ma}^{O_2}$, middle right) then follow $f_{int}^{O_2}$ closely. As interannual variations in sea–air CO$_2$ exchanges are much smaller than those in sea–air O$_2$ exchanges, the APO flux (Eq. (5); Fig. 7, top) dominantly reflects interannual variations in oxygen fluxes and thus in ocean-internal O$_2$ and DIC sources/sinks.

The APO flux inferred from SOCAT is compared to that inferred from atmospheric oxygen data by a transport inversion (Rödenbeck et al. (2008); five APO observation sites,
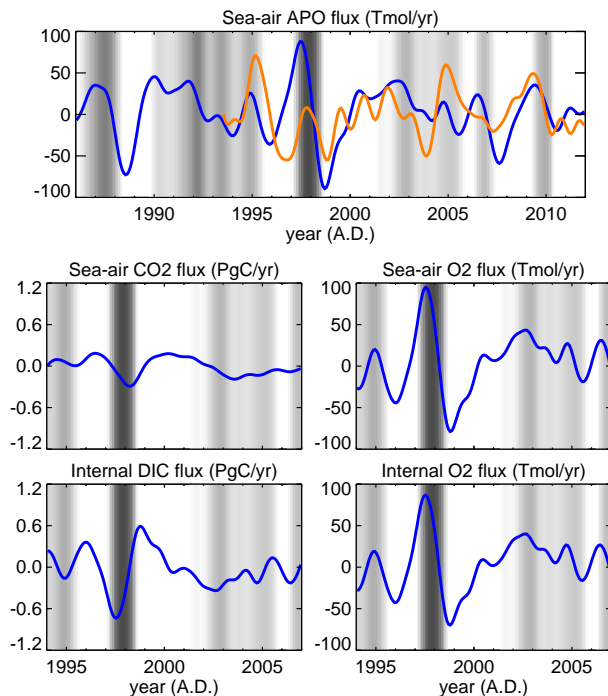
Figure 7. Top: interannual anomalies of the sea–air flux of atmospheric potential oxygen (APO) in the tropical Pacific, inferred from SOCAT (run **SFC**, blue) or independently estimated from atmospheric O$_2$ / N$_2$ ratios and CO$_2$ mixing ratios (atmospheric APO inversion, Rödenbeck et al. (2008); five sites, updated; orange). Temporal filter and sign conventions as in Fig. 3. The background shading indicates El Niño (MEI). Middle: sea–air fluxes of CO$_2$ and O$_2$ composing the APO flux (Eq. 5) for selected years for illustration. Bottom: ocean-internal sources and sinks of DIC and O$_2$. Vertical axes of all panels span the same range on a molar basis.

updated) (Fig. 7, top). Both of these mutually independent estimates show enhanced APO outgassing during El Niño phases (grey stripes; moderate correlations to the MEI exist both for the flux estimated from SOCAT (see Fig. 6) and the flux estimated by the APO inversion (see Rödenbeck et al., 2008)). While the SOCAT-based anomalies consistently lead ENSO events (due to the lead of f_{int}^{DIC}; compare Sect. 3.4), the APO-based anomalies coincide with the 1995 and 1997/1998 ENSO events but also lead the 2009 event. Both estimates are of roughly similar amplitudes (temporal standard deviations 1993–2008 of 33.7 Tmol yr^{-1} for run **SFC** and 28.9 Tmol yr^{-1} for the APO inversion), though the relative heights of the anomalies in individual ENSO events are markedly different.

Various conceivable error influences have the potential to distort the comparison:

(1) Both the SOCAT and the APO constraints suffer from incomplete spatial coverage, where the regions of good coverage do not necessarily coincide. An APO inversion of "synthetic data" suggests that the tropical Pacific may

be relatively well constrained, though the limited coverage may explain part of the differences in timing (Supplement, Sect. S5).

(2) The information flow from the SOCAT data (Fig. 2) involves various uncertain model steps: even if run **SFC** yielded a perfectly constrained $p_m^{CO_2}$ field, the fact would remain that the errors in the parameterizations of carbonate chemistry (CC) and carbon budget (CB) cause compensating spurious contributions to the internal f_{int}^{DIC} which then propagate to the calculated APO flux. A major simplification is the carbon–oxygen coupling (TT) assumed to be Redfieldian. Any errors in the oxygen budget (OB) and in the oxygen gas exchange (GE) contribute additionally, though their effect will be small due to the fast oxygen equilibration leading to $f_{ma}^{O_2} \approx f_{int}^{O_2}$ on interannual timescales.

(3) The APO inversion involves various uncertainties, both from necessary assumptions in the estimation and from observational error (Rödenbeck et al., 2008). Also, interannual variations in the sea–air N$_2$ exchange (influencing the APO inversion because the atmospheric O$_2$ abundance is measured relative to the N$_2$ abundance) are neglected.

In the light of all these error influences, but also considering that the SOCAT and APO constraints are fully independent from each other in terms of both data and model, the partial agreement in the interannual APO flux variations is noteworthy. Even though the comparison is not conclusive enough to provide a quantitative validation, we take it as a confirmation of plausibility of the mixed-layer scheme. Conversely, the comparison also confirms that atmospheric oxygen observations contain information about ocean-internal carbon sources/sinks and thus sea–air CO$_2$ exchange. To use this information as an additional constraint, we need to tackle the error influences listed above, in particular by:

– using a more realistic representation of carbon–oxygen coupling (TT). For this, the essential processes causing ocean-internal sources and sinks (making up contribution OIS) need to be suitably parameterized, for example explicit horizontal and vertical oceanic tracer transport. Potentially, further data sources would then be needed to separate processes with different carbon–oxygen relations.

– increasing the information from atmospheric oxygen by adding existing or new observation sites. A crucial role is played by the availability of atmospheric oxygen records that cover the entire time period under consideration without interruption.
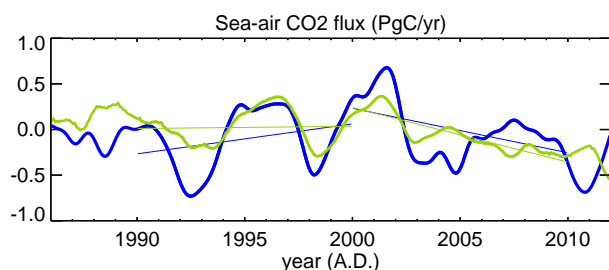
Figure 8. Interannual anomalies of the total ocean CO_2 flux estimated by run **SFC** (blue) and by the ocean process model run by Buitenhuis et al. (2010) (olive). Temporal filter and sign conventions as in Fig. 3. Linear fits of these results over the 1990–1999 and 2000–2009 periods are overplotted as thin lines.

3.6 Comparison to simulations by an ocean process model – IAV and trend

The data-based estimates presented here can be used to challenge the results of process simulations for well-constrained features, but conversely, comprehensive process models can be used to challenge our results where constraints are weak such that we rely on our simple parameterizations. Here we use the sea–air CO_2 fluxes simulated by the ocean biogeochemical process model PlankTOM5 (driven by NEMOv2.3; Buitenhuis et al., 2010). As in the SOCAT-based run **SFC**, the modelled total ocean flux variability (Fig. 8) is strongly tied to ENSO. Though the process model gives a smaller amplitude than **SFC** (about half), this model is the one with the largest interannual variability among the suite of process models considered in Wanninkhof et al. (2013) (their Fig. 6) and agrees by far the best with our SOCAT-based estimate.

In both the model simulation and our data-based run **SFC**, total ocean flux variability is dominated by the tropical Pacific, where both estimates are in even closer agreement than for the global total (Supplement, Fig. S2). The estimates further agree that all other regions have smaller IAV, though there is little correspondence in the detailed features. The regional comparison reveals that the differences in global amplitude are to a large extent related to areas south of the tropical Pacific, reinforcing the possibility that our amplitude is overestimated due to the tropical variability being spread over too great an area (end of Sect. 3.3). On the other hand, the comparison provides indications that the models with larger amplitude (as of Wanninkhof et al., 2013) may be more realistic than those with smaller amplitude.

Rising atmospheric CO_2 content leads to rising CO_2 undersaturation of the global ocean and thus an increasing oceanic sink. The magnitude of this trend, however, cannot be predicted from simple considerations as it critically depends on the rate by which the sequestered carbon is passed on from the surface ocean into the interior. Therefore process model simulations are needed. From a suite of models, Le Quéré et al. (2014) (Global Carbon Project, GCP) give a

sink time series increasing by $-0.032\,(\mathrm{Pg\,C\,yr^{-1}})\,\mathrm{yr^{-1}}$ over 1960–2012 (linear fit, converted to atmospheric sign convention). While the period of good data coverage is too short to compare this long-term trend, both our data-based estimates, NEMO-PlankTOM5, and the GCP model mean qualitatively agree that the 1990–1999 period saw a negligible or even reversed trend, followed by the 2000–2009 period with a trend almost 50 % stronger than the long-term one (trend lines in Fig. 8; see Fig. 5c of Le Quéré et al. (2014) for the temporal context). Unfortunately, a more quantitative analysis of these short-term trends is difficult due to the large interannual variability and region-to-region differences (e.g. Fay and McKinley, 2013).

3.7 Combination with an atmospheric CO_2 inversion – implication for land flux estimates

Interannual variations of regional sea–air CO_2 fluxes can also be estimated from atmospheric CO_2 mixing ratio measurements by atmospheric transport inversion (Newsam and Enting, 1988; Rayner et al., 1999). However, the atmospheric signal is dominated by the much larger variability of land–atmosphere CO_2 fluxes. Though the total (land and ocean) flux within latitude bands is relatively well constrained from atmospheric CO_2 data (due to atmospheric tracer mass conservation and the predominantly longitudinal tracer transport in the atmosphere), errors in the attribution to land or ocean, even if small compared to the land fluxes, can have a large relative impact on the smaller ocean fluxes. Indeed, we do not find much similarity between the SOCAT-based flux estimates and an atmospheric inversion (Fig. 9, top): the ocean total from the atmospheric inversion is almost anti-correlated to run **SFC** but rather more in phase with land biosphere variability (see Fig. 9, bottom), suggesting that these variations are spuriously spilling over from there. This is in line with a relatively large spread in the ocean fluxes from different atmospheric inversions (see the RECCAP[8] ensemble; Peylin et al., 2013), confirming a limited constraint of the atmospheric data on land–ocean flux partitioning. Similar discrepancies between SOCAT-based and atmospheric inversion estimates are also found in regional fluxes (Supplement, Fig. S3), though at least the relative amplitudes of flux IAV between the regions broadly agree. Surprisingly similar variations are found in the tropical Indian Ocean.

As the SOCAT-based estimates show more plausible ocean flux IAV than the atmospheric inversion, at least in the region contributing the largest variability (equatorial Pacific), it would be beneficial to add p^{CO_2} as a further constraint on the atmospheric inversion: due to the atmospheric mass conservation, land flux estimates profit from any improvement in the poorly constrained ocean fluxes. Even though interannual variations outside the equatorial Pacific are not well

---

[8]RECCAP is the "REgional Carbon Cycle Assessment and Processes" initiative of the Global Carbon Project.
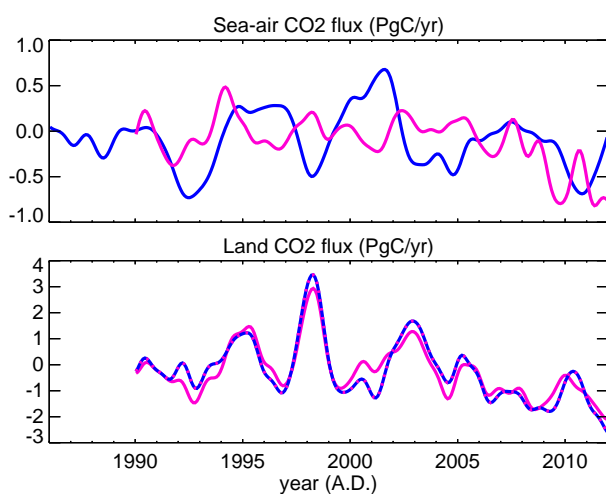
Figure 9. Top: interannual anomalies of the total ocean CO$_2$ flux estimated by run **SFC** (blue) and an atmospheric CO$_2$ inversion (magenta); temporal filter and sign conventions as in Fig. 3. Bottom: total land CO$_2$ flux estimated by an atmospheric CO$_2$ inversion (magenta – standard Jena inversion (s90_v3.5) with constant priors and ocean flux IAV being adjusted from the atmospheric data; dashed magenta/blue – atmospheric inversion using run **SFC** as fixed ocean prior). Note threefold vertical range in the land flux panel relative to ocean panel.

constrained from the p^{CO_2} data in many places and thus stay close to the prior of the diagnostic scheme (Sect. 3.2), they still contain the temperature-related part as represented in the parameterizations. In practical terms, even in areas where this is a bad approximation, using the SOCAT-based estimates will not worsen the land fluxes from the atmospheric inversion much (compared to an inversion with a freely adjustable ocean flux) due to their small amplitude. Only in the Southern Ocean, where influence from adjacent land regions is smallest, the constraint from atmospheric CO$_2$ data may be powerful and able to compensate for the weakness of the p^{CO_2} constraint there.

The inclusion of the p^{CO_2} constraint into the atmospheric inversion can be implemented by adding together the cost function contributions of the p^{CO_2} data and of the atmospheric CO$_2$ data (see the companion paper Rödenbeck et al. (2013), Appendix A2.3). However, as the ocean fluxes are much more strongly constrained by the p^{CO_2} data rather than the atmospheric data, such a joint inversion gives ocean fluxes almost identical to run **SFC** (test run not shown)[9]. Given this, we may simply use the results of run **SFC** as a fixed ocean prior in a subsequent "classical" atmospheric inversion in which only the land fluxes are adjusted, which is much more practical[10]. Figure 9 (bottom) compares total

---

[9]A similar situation was found in the joint inversion by Jacobson et al. (2007) considering long-term fluxes.

[10]The sequential estimation is much more efficient because the p^{CO_2} constraint needs many more iterations in the cost function

land CO$_2$ fluxes from atmospheric inversions with adjustable or fixed ocean fluxes. Using the SOCAT-based run **SFC** as prior slightly increases the land flux IAV. This is largely due to differences in South America (Supplement, Fig. S3) where the density of atmospheric measurement sites is low, such that the distinction of land and ocean fluxes is not well constrained in the "classical" atmospheric inversion. Differences also occur in the Asian regions. However, the impact is still roughly within the range of many other uncertainties in global atmospheric CO$_2$ inversions (e.g. see the spread of results by various inversion studies participating in the REC-CAP ensemble; Peylin et al., 2013).

Future developments of carbon cycle quantification should use the good constraint of p^{CO_2} data on the tropical Pacific and much of the northern extratropics but also the constraint of atmospheric CO$_2$ data on the Southern Ocean. Further, a joint CO$_2$ and APO inversion, linking sea–air CO$_2$ and O$_2$ fluxes through the diagnostic mixed-layer scheme, would exploit the potential of atmospheric oxygen observations to constrain the ocean-internal processes driving the sea–air CO$_2$ flux variability as demonstrated in Sect. 3.5 (test runs not shown). The APO constraint applies on the same large spatial scales that drive the sea–air CO$_2$ flux variability, and thus would be a valuable complement to the p^{CO_2} and atmospheric CO$_2$ data in the previously underconstrained areas.

4 Conclusions

Based on the SOCAT v2 data set of p^{CO_2} observations, we estimated interannual variations of the sea–air CO$_2$ exchange, using a data-driven diagnostic scheme of mixed-layer carbon biogeochemistry as a space–time interpolator. The scheme links sea–air CO$_2$ exchange to ocean-internal DIC sources and sinks, thereby also allowing us to relate carbon anomalies to signals in oxygen (or nutrient) observations.

– SOCAT p^{CO_2} data constrain interannual variations in the sea–air CO$_2$ flux in parts of the ocean, notably in the tropical Pacific where the largest interannual variations are found.

– The tropical Pacific shows a reduced CO$_2$ outgassing during El Niño phases. In the east, this anomaly occurs more than 6 months later than in the west, likely due to different relative contributions of temperature-related and biologically/physically caused responses.

– The SOCAT-based estimates of the interannual variations in tropical sea–air CO$_2$ flux and ocean-internal DIC sources/sinks are broadly consistent with the

---

minimization (about 200) than the atmospheric inversion (about 70). A combined inversion would require the expensive transport model runs for all these additional iterations.

independent constraint from atmospheric oxygen measurements.

– In qualitative agreement with ocean process model simulations, the ocean sink in the SOCAT-based estimates increased less than expected from an atmospheric CO_2 rise during 1990–1999 and more than expected during 2000–2009.

– Surface-ocean p^{CO_2} data constrain interannual variations in sea–air CO_2 fluxes better than atmospheric CO_2 data, at least for the dominating variations in the tropical Pacific. The p^{CO_2}-based estimates can be used as an ocean prior in atmospheric CO_2 inversions to improve their land flux estimates.

The presented gridded sea–air CO_2 flux estimates can be downloaded in digital form from the Jena inversion website: http://www.bgc-jena.mpg.de/~christian.roedenbeck/download-CO2-ocean/ (version "oc_v1.2"). Regular updates are planned.

The Supplement related to this article is available online at doi:10.5194/bg-11-4599-2014-supplement.

References

Anderson, L.: On the hydrogen and oxygen content of marine phytoplankton, Deep-Sea Res. Pt. I, 42, 1675–1680, 1995.

Arthun, M., Bellerby, R. G. J., Omar, A. M., and Schrum, C.: Spatiotemporal variability of air-sea CO_2 fluxes in the Barents Sea, as determined from empirical relationships and modeled hydrography, J. Mar. Syst., 98–99, 40–50, doi:10.1016/j.jmarsys.2012.03.005, 2012.

Bakker, D. C. E., Pfeil, B., Smith, K., Hankin, S., Olsen, A., Alin, S. R., Cosca, C., Harasawa, S., Kozyr, A., Nojiri, Y., O'Brien, K. M., Schuster, U., Telszewski, M., Tilbrook, B., Wada, C., Akl, J., Barbero, L., Bates, N. R., Boutin, J., Bozec, Y., Cai, W.-J., Castle, R. D., Chavez, F. P., Chen, L., Chierici, M., Currie, K., de Baar, H. J. W., Evans, W., Feely, R. A., Fransson, A., Gao, Z., Hales, B., Hardman-Mountford, N. J., Hoppema, M., Huang, W.-J., Hunt, C. W., Huss, B., Ichikawa, T., Johannessen, T., Jones, E. M., Jones, S. D., Jutterström, S., Kitidis, V., Körtzinger, A., Landschützer, P., Lauvset, S. K., Lefèvre, N., Manke, A. B., Mathis, J. T., Merlivat, L., Metzl, N., Murata, A., Newberger, T., Omar, A. M., Ono, T., Park, G.-H., Paterson, K., Pierrot, D., Ríos, A. F., Sabine, C. L., Saito, S., Salisbury, J., Sarma, V. V. S. S., Schlitzer, R., Sieger, R., Skjelvan, I., Steinhoff, T., Sullivan, K. F., Sun, H., Sutton, A. J., Suzuki, T., Sweeney, C., Takahashi, T., Tjiputra, J., Tsurushima, N., van Heuven, S. M. A. C., Vandemark, D., Vlahos, P., Wallace, D. W. R., Wanninkhof, R., and Watson, A. J.: An update to the Surface Ocean CO_2 Atlas (SOCAT version 2), Earth Syst. Sci. Data, 6, 69–90, doi:10.5194/essd-6-69-2014, 2014.

Bates, N. R., Best, M. H. P., Neely, K., Garley, R., Dickson, A. G., and Johnson1, R. J.: Detecting anthropogenic carbon dioxide uptake and ocean acidification in the North Atlantic Ocean, Biogeosciences, 9, 2509–2522, doi:10.5194/bg-9-2509-2012, 2012.

Buitenhuis, E., Rivkin, R., Sailley, S., and Le Quéré, C.: Biogeochemical fluxes through microzooplankton, Global Biogeochem. Cy., 24, GB4015, doi:10.1029/2009GB003601, 2010.

Chevallier, F., Bréon, F.-M., and Rayner, P. J.: Contribution of the Orbiting Carbon Observatory to the estimation of CO2 sources and sinks: Theoretical study in a variational data assimilation framework, J. Geophys. Res., 112, D09307, doi:10.1029/2006JD007375, 2007.

Conkright, M., Locarnini, R. A., Garcia, H., O'Brien, T., Boyer, T., Stephens, C., and Antonov, J.: World Ocean Atlas 2001: Objective Analyses, Data Statistics, and Figures, CD-ROM Documentation, National Oceanographic Data Center, Silver Spring, MD, 17 pp., 2002.

Corbière, A., Metzl, N., Reverdin, G., Brunet, C., and Takahashi, T.: Interannual and decadal variability of the oceanic carbon sink in the North Atlantic subpolar gyre, Tellus B, 59, 168–178, 2007.

de Boyer Montégut, C., Madec, G., Fischer, A. S., Lazar, A., and Iudicone, D.: Mixed layer depth over the global ocean: an examination of profile data and a profile-based climatology, J. Geophys. Res., 109, C12003, doi:10.1029/2004JC002378, 2004.

Dore, J., Lukas, R., Sadler, D., Church, M., and Karl, D.: Physical and biogeochemical modulation of ocean acidification in the central North Pacific, P. Natl. Acad. Sci. USA, 106, 12235–12240, 2009.

Egleston, E. S., Sabine, C. L., and Morel, F. M. M.: Revelle revisited: Buffer factors that quantify the response of ocean chemistry

to changes in DIC and alkalinity, Global Biogeochem. Cy., 24, GB1002, doi:10.1029/2008GB003407, 2010.

Fay, A. R. and McKinley, G. A.: Global trends in surface ocean pCO$_2$ from in situ data, Global Biogeochem. Cy., 27, 541–557, doi:10.1002/gbc.20051, 2013.

Feely, R., Boutin, J., Cosca, C., Dandonneau, Y., Etcheto, J., Inoue, H., Ishii, M., Quéré, C. L., Mackey, D., McPhaden, M., Metzl, N., Poisson, A., and Wanninkhov, R.: Seasonal and Interannual Variability of CO$_2$ in the Equatorial Pacific, Deep-Sea Res. Pt. II, 49, 2443–2469, doi:10.1016/S0967-0645(02)00044-9, 2002.

Feely, R. A., Wanninkhof, R., Takahashi, T., and Tans, P.: Influence of El Niño on the equatorial Pacific contribution to atmospheric CO$_2$ accumulation, Nature, 398, 597–601, 1999.

Garcia, H. E., Locarnini, R. A., Boyer, T. P., and Antonov, J. I.: World Ocean Atlas 2005, Volume 3: Dissolved Oxygen, Apparent Oxygen Utilization, and Oxygen Saturation, in: NOAA Atlas NESDIS 63, edited by: Levitus, S., U.S. Government Printing Office, Washington, DC, 2006.

Inoue, H., Ishii, M., Matsueda, H., Saito, S., Aoyama, M., Tokieda, T., Midorikawa, T., Nemoto, K., Kawano, T., Asanuma, I., Ando, K., Yano, T., and Murata, A.: Distributions and variations in the partial pressure of CO$_2$ in surface waters (pCO$_2^w$) of the central and western equatorial Pacific during the 1997/1998 El Niño event, Mar. Chem., 76, 59–75, 2001.

Ishii, M., Feely, R. A., Rodgers, K. B., Park, G.-H., Wanninkhof, R., Sasano, D., Sugimoto, H., Cosca, C. E., Nakaoka, S., Telszewski, M., Nojiri, Y., Fletcher, S. E. M., Niwa, Y., Patra, P. K., Valsala, V., Nakano, H., Lima, I., Doney, S. C., Buitenhuis, E. T., Aumont, O., Dunne, J. P., Lenton, A., and Takahashi, T.: Air-sea CO$_2$ flux in the Pacific Ocean for the period 1990-2009, Biogeosciences, 11, 709–734, doi:10.5194/bg-11-709-2014, 2014.

Jacobson, A. R., Mikaloff Fletcher, S. E., Gruber, N., Sarmiento, J. L., and Gloor, M.: A joint atmosphere-ocean inversion for surface fluxes of carbon dioxide: 1. Methods and global-scale fluxes, Global Biogeochem. Cy., 21, GB1019, doi:10.1029/2005GB002556, 2007.

Kalnay, E., Kanamitsu, M., Kistler, R., Collins, W., Deaven, D., Gandin, L., Iredell, M., Saha, S., White, G., Woollen, J., Zhu, Y., Chelliah, M., Ebisuzaki, W., Higgins, W., Janowiak, J., Mo, K. C., Ropelewski, C., Wang, J., Leetmaa, A., Reynolds, R., Jenne, R., and Joseph, D.: The NCEP/NCAR 40-year reanalysis project, B. Am. Meteorol. Soc., 77, 437–471, 1996.

Keeling, R. F.: Development of an interferometric oxygen analyzer for precise measurement of the atmospheric O$_2$ mole fraction, Ph.D. thesis, Harvard Univ., Cambridge, USA, 1988.

Keeling, R. F. and Shertz, S. R.: Seasonal and interannual variations in atmospheric oxygen and implications for the global carbon cycle, Nature, 358, 723–727, 1992.

Key, R. M., Kozyr, A., Sabine, C. L., Lee, K., Wanninkhof, R., Bullister, J. L., Feely, R. A., Millero, F. J., Mordy, C., and Peng, T.-H.: A global ocean carbon climatology: Results from Global Data Analysis Project (GLODAP), Global Biogeochem. Cy., 18, GB4031, doi:10.1029/2004GB002247, 2004.

Landschützer, P., Gruber, N., Bakker, D., Schuster, U., Nakaoka, S., Payne, M., Sasse, T., and Zeng, J.: A neural network-based estimate of the seasonal to inter-annual variability of the Atlantic Ocean carbon sink, Biogeosciences, 10, 7793–7815, doi:10.5194/bg-10-7793-2013, 2013.

Lee, K., Tong, L. T., Millero, F. J., Sabine, C. L., Dickson, A. G., Goyet, C., Park, G.-H., Wanninkhof, R., Feely, R. A., and Key, R. M.: Global relationships of total alkalinity with salinity and temperature in surface waters of the world's oceans, Geophys. Res. Lett., 33, L19605, doi:10.1029/2006GL027207, 2006.

Le Quéré, C., Peters, G. P., Andres, R. J., Andrew, R. M., Boden, T. A., Ciais, P., Friedlingstein, P., Houghton, R. A., Marland, G., Moriarty, R., Sitch, S., Tans, P., Arneth, A., Arvanitis, A., Bakker, D. C. E., Bopp, L., Canadell, J. G., Chini, L. P., Doney, S. C., Harper, A., Harris, I., House, J. I., Jain, A. K., Jones, S. D., Kato, E., Keeling, R. F., Klein Goldewijk, K., Körtzinger, A., Koven, C., Lefèvre, N., Maignan, F., Omar, A., Ono, T., Park, G.-H., Pfeil, B., Poulter, B., Raupach, M. R., Regnier, P., Rödenbeck, C., Saito, S., Schwinger, J., Segschneider, J., Stocker, B. D., Takahashi, T., Tilbrook, B., van Heuven, S., Viovy, N., Wanninkhof, R., Wiltshire, A., and Zaehle, S.: Global carbon budget 2013, Earth Syst. Sci. Data, 6, 235–263, doi:10.5194/essd-6-235-2014, 2014.

McKinley, G. A., Fay, A. R., Takahashi, T., and Metzl, N.: Convergence of atmospheric and North Atlantic carbon dioxide trends on multidecadal timescales, Nat. Geosci., 4, 606–610, 2011.

Metzl, N., Corbière, A., Reverdin, G., Lenton, A., Takahashi, T., Olsen, A., Johannessen, T., Pierrot, D., Wanninkhof, R., Ólafsdóttir, S. R., Olafsson, J., and Ramonet, M.: Recent acceleration of the sea surface fCO2 growth rate in the North Atlantic subpolar gyre (1993–2008) revealed by winter observations, Global Biogeochem. Cy., 24, GB4004, doi:10.1029/2009GB003658, 2010.

Monahan, E. C. and Torgersen, T.: Enhancement of air-sea gas exchange by oceanic whitecapping, in: Air-Water Mass Transfer: Selected Papers from the Second International Symposium on Gas Transfer at Water Surfaces, edited by: Wilhelms, S. C. and Gulliver, J. S., 608–617, Am. Soc. of Civ. Eng., New York, 1990.

Naegler, T.: Reconciliation of excess ^{14}C-constrained global CO$_2$ piston velocity estimates, Tellus B, 61, 372–384, 2009.

Newsam, G. N. and Enting, I. G.: Inverse problems in atmospheric constituent studies: I. Determination of surface sources under a diffusive transport approximation, Inverse Problems, 4, 1037–1054, 1988.

Park, G.-H., Wanninkhof, R., Doney, S. C., Takahashi, T., Lee, K., Feely, R. A., Sabine, C. L., Triñanes, J., and Lima, I. D.: Variability of global net sea-air CO$_2$ fluxes over the last three decades using empirical relationships, Tellus B, 62, 352–368, 2010.

Peylin, P., Law, R. M., Gurney, K. R., Chevallier, F., Jacobson, A. R., Maki, T., Niwa, Y., Patra, P. K., Peters, W., Rayner, P. J., Rödenbeck, C., van der Laan-Luijkx, I. T., and Zhang, X.: Global atmospheric carbon budget: results from an ensemble of atmospheric CO$_2$ inversions, Biogeosciences, 10, 6699–6720, doi:10.5194/bg-10-6699-2013, 2013.

Pfeil, B., Olsen, A., Bakker, D. C. E., Hankin, S., Koyuk, H., Kozyr, A., Malczyk, J., Manke, A., Metzl, N., Sabine, C. L., Akl, J., Alin, S. R., Bates, N., Bellerby, R. G. J., Borges, A., Boutin, J., Brown, P. J., Cai, W.-J., Chavez, F. P., Chen, A., Cosca, C., Fassbender, A. J., Feely, R. A., González-Dávila, M., Goyet, C., Hales, B., Hardman-Mountford, N., Heinze, C., Hood, M., Hoppema, M., Hunt, C. W., Hydes, D., Ishii, M., Johannessen, T., Jones, S. D., Key, R. M., Körtzinger, A., Landschützer, P., Lauvset, S. K., Lefèvre, N., Lenton, A., Lourantou, A., Merlivat, L., Midorikawa, T., Mintrop, L., Miyazaki, C., Murata, A., Naka-

date, A., Nakano, Y., Nakaoka, S., Nojiri, Y., Omar, A. M., Padin, X. A., Park, G.-H., Paterson, K., Perez, F. F., Pierrot, D., Poisson, A., Ríos, A. F., Santana-Casiano, J. M., Salisbury, J., Sarma, V. V. S. S., Schlitzer, R., Schneider, B., Schuster, U., Sieger, R., Skjelvan, I., Steinhoff, T., Suzuki, T., Takahashi, T., Tedesco, K., Telszewski, M., Thomas, H., Tilbrook, B., Tjiputra, J., Vandemark, D., Veness, T., Wanninkhof, R., Watson, A. J., Weiss, R., Wong, C. S., and Yoshikawa-Inoue, H.: A uniform, quality controlled Surface Ocean CO$_2$ Atlas (SOCAT), Earth Syst. Sci. Data, 5, 125–143, doi:10.5194/essd-5-125-2013, 2013.

Rayner, P., Enting, I., Francey, R., and Langenfelds, R.: Reconstructing the recent carbon cycle from atmospheric CO$_2$, δ^{13}CO$_2$ and O$_2$/N$_2$ observations, Tellus B, 51, 213–232, 1999.

Rödenbeck, C.: Estimating CO$_2$ sources and sinks from atmospheric mixing ratio measurements using a global inversion of atmospheric transport, Tech. Rep. 6, Max Planck Institute for Biogeochemistry, Jena, Germany, 2005.

Rödenbeck, C., Le Quéré, C., Heimann, M., and Keeling, R.: Interannual variability in oceanic biogeochemical processes inferred by inversion of atmospheric O$_2$/N$_2$ and CO$_2$ data, Tellus B, 60, 685–705, 2008.

Rödenbeck, C., Keeling, R. F., Bakker, D. C. E., Metzl, N., Olsen, A., Sabine, C., and Heimann, M.: Global surface-ocean pCO$_2$ and sea–air CO$_2$ flux variability from an observation-driven ocean mixed-layer scheme, Ocean Sci., 9, 193–216, doi:10.5194/os-9-193-2013, 2013.

Sabine, C., Maenner, S., and Sutton, A.: High-resolution ocean and atmosphere pCO$_2$ time-series measurements from mooring TAO140W, doi:10.3334/CDIAC/otg.TSM_TAO140W, available at: http://cdiac.esd.ornl.gov/ftp/oceans/Moorings/TAO140W/, 2010.

Santoso, A., McGregor, S., Jin, F.-F., Cai, W., England, M. H., An, S.-I., McPhaden, M. J., and Guilyardi, E.: Late-twentieth-century emergence of the El Niño propagation asymmetry and future projections, Nature, 504, 126–130, doi:10.1038/nature12683, 2013.

Sarmiento, J. L. and Gruber, N.: Ocean Biogeochemical Dynamics, Princeton Univ. Press, 2006.

Sarmiento, J. L., Gloor, E., Gruber, N., Beaulieu, C., Jacobson, A. R., Fletcher, S. E. M., Pacala, S., and Rodgers, K.: Trends and Regional Distributions of Land and Ocean Carbon Sinks, Biogeosciences, 7, 2351–2367, doi:10.5194/bg-7-2351-2010, 2010.

Schuster, U., McKinley, G. A., Bates, N., Chevallier, F., Doney, S. C., Fay, A. R., González-Dávila, M., Gruber, N., Jones, S., Krijnen, J., Landschützer, P., Lefèvre, N., Manizza, M., Mathis, J., Metzl, N., Olsen, A., Rios, A. F., Rödenbeck, C., Santana-Casiano, J. M., Takahashi, T., Wanninkhof, R., and Watson, A. J.: Atlantic and Arctic sea-air CO$_2$ fluxes, 1990–2009, Biogeosciences, 10, 607–627, doi:10.5194/bg-10-607-2013, 2013.

Stanley, R. H. R., Jenkins, W. J., Lott III, D. E., and Doney, S. C.: Noble gas constraints on air-sea gas exchange and bubble fluxes, J. Geophys. Res., 114, C11020, doi:10.1029/2009JC005396, 2009.

Stephens, B. B., Keeling, R. F., Heimann, M., Six, K. D., Murnane, R., and Caldeira, K.: Testing global ocean carbon cycle models using measurements of atmospheric O$_2$ and CO$_2$ concentration, Global Biogeochem. Cy., 12, 213–230, 1998.

Takahashi, T., Sutherland, S. C., Wanninkhof, R., Sweeney, C., Feely, R. A., Chipman, D. W., Hales, B., Friederich, G., Chavez, F., Sabine, C., Watson, A., Bakker, D. C. E., Schuster, U., Metzl, N., Yoshikawa-Inoue, H., Ishii, M., Midorikawa, T., Nojiri, Y., Körtzinger, A., Steinhoff, T., Hoppema, M., Olafsson, J., Arnarson, T. S., Tillbrook, B., Johannessen, T.and Olsen, A., Bellerby, R., Wong, C. S., Delille, B., Bates, N. R., and de Baar, H. J. W.: Climatological mean and decadal change in surface ocean pCO$_2$ and net sea-air CO$_2$ flux over the global oceans, Deep-Sea Res. Pt. II, 56, 554–577, 2009.

Tarantola, A.: Inverse Problem Theory, Methods for Data Fitting and Model Parameter Estimation, Elsevier, New York, 1987.

Telszewski, M., Chazottes, A., Schuster, U., Watson, A., Moulin, C., Bakker, D., González-Dávila, M., Johannessen, T., Körtzinger, A., Lüger, H., Olsen, A., Omar, A., Padin, X., Ríos, A., Steinhoff, T., Santana-Casiano, M., Wallace, D. W. R., and Wanninkhof, R. H.: Estimating the monthly pCO$_2$ distribution in the North Atlantic using a self-organizing neural network, Biogeosciences, 6, 1405–1421, doi:10.5194/bg-6-1405-2009, 2009.

Wanninkhof, R.: Relationship between wind speed and gas exchange over the ocean, J. Geophys. Res.-Oceans, 97, 7373–7382, 1992.

Wanninkhof, R., Park, G. H., Takahashi, T., Sweeney, C., Feely, R., Nojiri, Y., Gruber, N., Doney, S. C., McKinley, G. A., Lenton, A., Le Quéré, C., Heinze, C., Schwinger, J., Graven, H., and Khatiwala, S.: Global ocean carbon uptake: magnitude, variability and trends, Biogeosciences, 10, 1983–2000, doi:10.5194/bg-10-1983-2013, 2013.

Watson, A. J., Schuster, U., Bakker, D. C. E., Bates, N. R., Corbiére, A., González-Dávila, M., Friedrich, T., Hauck, J., Heinze, C., Johannessen, T., Körtzinger, A., Metzl, N., Olafsson, J., Olsen, A., Oschlies, A., Padin, X. A., Pfeil, B., Santana-Casiano, J. M., Steinhoff, T., Telszewski, M., Rios, A. F., Wallace, D. W. R., and Wanninkhof, R.: Tracking the Variable North Atlantic Sink for Atmospheric CO$_2$, Science, 326, 1391–1393, doi:10.1126/science.1177394, 2009.

Weiss, R.: Carbon dioxide in water and seawater: the solubility of a non-ideal gas, Mar. Chem., 2, 203–205, 1974.

Wolter, K. and Timlin, M.: Monitoring ENSO in COADS with a seasonally adjusted principal component index, Proc. of the 17th Climate Diagnostics Workshop, Norman, OK, NOAA/N MC/CAC, NSSL, Oklahoma Clim. Survey, CIMMS and the School of Meteor., Univ. of Oklahoma, 52–57, 1993.

Yu, L. and Weller, R. A.: Objectively Analyzed air-sea heat Fluxes (OAFlux) for the global oceans, B. Am. Meteorol. Soc., 88, 527–539, 2007.